drones

MDPI

Article

Fixed-Time Extended Observer-Based Adaptive Sliding Mode Control for a Quadrotor UAV under Severe Turbulent Wind

Armando Miranda-Moya [1], Herman Castañeda [1,*] and Hesheng Wang [2]

[1] Tecnologico de Monterrey, School of Sciences and Engineering, Monterrey 64849, Mexico; a00823922@tec.mx
[2] Department of Automation, Key Laboratory of System Control and Information Processing of Ministry of Education, Key Laboratory of Marine Intelligent Equipment and System of Ministry of Education, Shanghai Engineering Research Center of Intelligent Control and Management, Shanghai Jiao Tong University, Shanghai 200240, China; wanghesheng@sjtu.edu.cn
* Correspondence: hermancc@tec.mx

Abstract: This paper presents a fixed-time extended state observer-based adaptive sliding mode controller evaluated in a quadrotor unmanned aerial vehicle subject to severe turbulent wind while executing a desired trajectory. Since both the state and model of the system are assumed to be partially known, the observer, whose convergence is independent from the initial states of the system, estimates the full state, model uncertainties, and the effects of turbulent wind in fixed time. Such information is then compensated via feedback control conducted by a class of adaptive sliding mode controller, which is robust to perturbations and reduces the chattering effect by non-overestimating its adaptive gain. Furthermore, the stability of the closed-loop system is analyzed by means of the Lyapunov theory. Finally, simulation results validate the feasibility and advantages of the proposed strategy, where the observer enhances performance. For further demonstration, a comparison with an existent approach is provided.

Keywords: fixed-time extended state observer; adaptive sliding mode control; robust control; disturbance rejection; wind turbulence; quadrotor UAV

Citation: Miranda-Moya, A.; Castañeda, H.; Wang, H. Fixed-Time Extended Observer-Based Adaptive Sliding Mode Control for a Quadrotor UAV under Severe Turbulent Wind. *Drones* **2023**, *7*, 700. https://doi.org/10.3390/drones7120700

Academic Editor: Andrey V. Savkin

Received: 22 October 2023
Revised: 27 November 2023
Accepted: 28 November 2023
Published: 9 December 2023

1. Introduction

External disturbances due to wind produce adverse effects on quadrotor unmanned aerial vehicles (UAVs) when flying outdoors. Depending on its intensity, the rotorcraft can suffer from small erratic movements to complete system instability. To avoid the latter, advanced robust control strategies such as [1–5] have been proposed to handle the nonlinearities of the UAV in perturbed conditions. However, their rejection against strong enough disturbances tends to be slow since it relies on a feedback regulation defined by the error between the states of the quadrotor and their respective setpoints [6]. Moreover, it has been proven in [7,8] that the vehicle can maintain its flight stability but cannot execute proper trajectory tracking. Thus, approaches such as [9–12] employ a disturbance rejection method where the total disturbance affecting the system is estimated through a disturbance observer and later compensated on the control inputs of the robot.

Frequently, external perturbations are established as step or periodic functions [13–17]. However, such functions do not reflect the actual wind dynamics. Although wind evolution is hard to describe mathematically due to its random conduct, the US Military standard MIL-STD-1797A [18] endorses the Dryden and Von Karman wind models to analyze the performance of aerial vehicles in environments that involve turbulent air behavior at different altitude levels. These numerical approximations are implemented in Rodriguez-Mata et al. [19] where a nonlinear high-gain disturbance observer-based PD attitude controller is designed for a quadrotor UAV. The effects of the wind disturbances represented by the Dryden model are analyzed through the evolution of the torque of the motors. In Zhang et al. [20], disturbance observer-based backstepping and sliding mode controllers are developed to manage the linear and angular dynamics of a

rotorcraft, respectively. Furthermore, the approaches from Aboudonia et al. [21,22] present a disturbance observer-linear feedback control scheme for a quadrotor UAV susceptible to mismatched perturbations. The low-altitude turbulent wind effects are analyzed in the mathematical model of the rotorcraft as drag forces that actuate over the vehicle. Moreover, the same authors propose a disturbance observer-sliding mode strategy for a quadrotor UAV considering partial motor failure. The wind turbulent field given by the Von Karman model is also analyzed in the form of drag forces [23].

Previous designs require the complete knowledge of the full-state measurements of the system which may not be available due to a lack of instruments or sensor noise conditions. Then, in [24], Han proposes an active disturbance rejection controller where an extended state observer (ESO) provides estimations of both the full-state and slow time-varying perturbations and uncertainties by adding an extra state to the mathematical model of the plant. Following the prior approach, the authors of [25] propose a backstepping-sliding mode strategy to control a quadrotor using the measurement and disturbance estimations from a linear ESO. Additionally, Shao et al. [26] introduce an ESO-based dynamic surface controller that improves the performance of a backstepping scheme. However, its robustness against external disturbances can still be enhanced by employing a sliding mode controller instead. Then, in ref. [27], the authors present a nonlinear extended state observer-based fuzzy sliding mode technique to drive the pose of a rotorcraft. Considering a first-order sliding method as the auxiliary controller, a fuzzy logic approach is implemented to attenuate the chattering of the control inputs of the vehicle. Nonetheless, the effectiveness of this strategy in reducing the chattering effect strongly depends on an appropriate number of fuzzy rules and heuristics which may not provide results as good as a defined adjustment function.

On the other hand, to guarantee the complete stability of the quadrotor UAV under an observer-based control scheme, the convergence of the observer must be much faster than the convergence of the controller. Extended state observers with asymptotic and finite-time equilibrium achievement are proposed in [28,29], respectively. Even though finite-time strategies offer a better performance regarding estimation and error reduction, their convergence time increases as the initial conditions of the error of the system rise. In addition, these values could be unknown during practice. As a solution, in [30], Polyakov introduces a fixed-time stable system whose convergence is independent from its initial conditions. This approach has been adopted for the design of ESO-based controllers in [31–34]. In that sense, Mechali et al. [35] make a complete analysis of the feasibility of fixed-time ESO-based terminal sliding mode schemes for the position and attitude driving of a quadrotor UAVs subject to external disturbances described by the Dryden wind model. Similarly, Li et al. [36] introduce a fixed-time ESO-based dynamic surface control whose design follows a fast terminal sliding mode approach. Nevertheless, different from real conditions, the authors consider external disturbances in the form of periodic functions only. Finally, Liu et al. [37] present the design of an ESO-based algorithm for a fixed-wing UAV. The observer is employed to estimate the uncertainties that affect the vehicle when performing a high angle of attack. Nonetheless, prior approaches rely on fixed-gain control strategies with heuristically chosen parameters. This may lead to the implementation of larger gains than necessary, resulting in excessive energy delivery and possible overfitting of the controller. To avoid the latter, adaptive strategies can be designed to provide the proper amount of control effort to the system without overestimating the control parameters.

Then, the main contribution of this paper relies on the design of a fixed-time extended state observer (FxtESO)-based adaptive sliding mode controller (ASMC) for a quadrotor UAV subject to severe wind turbulent gusts described by the Von Karman model. Through the assumption of partial state measurements, the FxtESO provides estimations regarding the full state of the UAV, the complex random behavior of the turbulent wind gust, and model uncertainties in fixed time, independently of the initial state and without complete knowledge of the system. The flight control is performed by the ASMC, which offers properties such as robustness against bounded external perturbations and uncertainties,

chattering attenuation due to the adjustment of its adaptive gain, and practical finite-time state convergence. Furthermore, the closed-loop stability of the system is guaranteed through an analysis based on the Lyapunov theory. Simulation results demonstrate the improvements in the performance of the rotorcraft due to the implementation of the observer. Moreover, the effectiveness and advantages such as robustness, estimation of the full state and perturbations and its adaptive control gain, which modulates the control input as needed of the proposed approach are compared with an existing observed-based control methodology.

The paper is divided as follows: Section 2 addresses the dynamics of the quadrotor UAV and the Von Karman turbulent wind model. The design of the FxtESO-based ASMC scheme is described in Section 3. Simulation results are revealed and discussed in Section 4. Finally, the conclusions are presented in Section 5.

2. Preliminaries

The definitions and lemmas that sustain the FxtESO-based ASMC scheme are addressed. First, we assume a scalar state $x \in \mathbb{R}$ and a nonlinear function $\text{sig}^r(x) = |x|^r \text{sign}(x)$, with $r \in (0,1)$, $|x|$ as the absolute value of x, and

$$\text{sign}(x) = \begin{cases} -1 & \text{if } x < 0 \\ 0 & \text{if } x = 0 \\ 1 & \text{if } x > 0 \end{cases}. \tag{1}$$

Now, we consider the following single-input single-output (SISO) nonlinear system with control input $\mathrm{U} \in \mathbb{R}$:

$$\dot{x} = f(x, \mathrm{U}), \;\; x_0 = x(t_0). \tag{2}$$

Definition 1 ([38]). *The equilibrium point $x = 0$ is asymptotically stable if there is a continuously differentiable function $\mathcal{V}$ that fulfills $\mathcal{V}(0) = 0$, and $\mathcal{V} > 0$, $\dot{\mathcal{V}} < 0$ for all $x - \{0\}$ that exists in the domain of solutions of* (2).

Definition 2 ([39]). *The origin of* (2) *is finite-time stable if it is asymptotically stable and any solution of the system achieves the equilibrium point $x = 0$ after a time $T_m(x_0)$. In other words, $x(t, x_0) = 0$, $\forall t \geq T_m(x_0)$.*

Definition 3 ([40]). *The solution of system* (2) *is said to be practical finite-time stable if, with $\forall x_0$, there is value $\Gamma > 0$ and time $T_k(\Gamma, x_0) < \infty$ that satisfy $|x(t)| < \Gamma$, $\forall t \geq t_0 + T_k(\Gamma, x_0)$*

Definition 4 ([41,42]). *The origin of* (2) *is fixed-time stable if it is globally finite-time stable and there is a bounded settling time function $T_f(x)$ such that $0 < T_f \leq T_{max}$.*

Lemma 1 ([43]). *System*

$$\begin{aligned} \dot{\vartheta}_1 &= \vartheta_2 - \varkappa_1 |\vartheta_1|^{\varpi_1} sign(\vartheta_1) \\ \dot{\vartheta}_2 &= \vartheta_3 - \varkappa_2 |\vartheta_1|^{\varpi_2} sign(\vartheta_1) \\ &\vdots \\ \dot{\vartheta}_{n-1} &= \vartheta_n - \varkappa_{n-1} |\vartheta_1|^{\varpi_{n-1}} sign(\vartheta_1) \\ \dot{\vartheta}_n &= -\varkappa_n |\vartheta_1|^{\varpi_n} sign(\vartheta_1) \\ \varpi_1 &= \bar{\varpi} \end{aligned}$$

is homogeneous of degree $\bar{\varpi} - 1$ with respect to weights $\{(i-1)\bar{\varpi} - (i-2)\}$ for $1 \leq i \leq n$ and $\varpi_i = i\bar{\varpi} - (i-1)$ for $2 \leq i \leq n$, if $\bar{\varpi} > 1 - \frac{1}{n-1}$.

Lemma 2 ([44]). *We assume that vector field v_f is homogeneous of degree k with respect to vector field v_g. Then, the origin is a finite-time-stable equilibrium under v_f if and only if the origin is an asymptotically stable equilibrium under v_f and $k < 0$.*

Lemma 3 ([30]). *We assume that there is a continuous unbounded function V. We set $\Theta_s \subset \mathbb{R}^n$; it is globally fixed-time attractive if $V(q) = 0 \Rightarrow q \in \Theta_s$ and any $q(t)$ satisfies $\dot{V}(q) \leq -(\alpha V^a(q(t)) + \beta V^b(q(t)))^c$ for $\alpha, \beta, a, b, c > 0$, with $ac < 1$, $bc > 1$, and settling time function*

$$T_f \leq \frac{1}{\alpha^c(1-ac)} + \frac{1}{\beta^c(bc-1)}. \tag{3}$$

Lemma 4 ([40,45]). *We consider system (2) and suppose that there is a continuous function $\mathcal{V}(x)$ that fulfills $\mathcal{V}(0) = 0$ and $\mathcal{V}(x) \in \mathbb{R}^+, \forall x \neq 0$. Then, the origin of (2) is practical finite-time stable if*

$$\dot{\mathcal{V}}(x) \leq -h\mathcal{V}(x)^{\mathcal{L}} + \mathcal{W}, \tag{4}$$

where $h, \mathcal{W} > 0$ and $0 < \mathcal{L} < 1$. Moreover, the trajectories of x are bounded in finite-time as

$$\lim_{\mathcal{Y} \to \mathcal{Y}_0} x \in \left(\mathcal{V}^{\mathcal{L}}(x) \leq \frac{\mathcal{W}}{(1-\mathcal{L})h}\right), \tag{5}$$

with $0 < \mathcal{Y} \leq 1$, $0 < \mathcal{Y}_0 < 1$ and settling time function

$$T_k \leq \frac{\mathcal{V}^{1-\mathcal{L}}(x_0)}{h\mathcal{Y}_0(1-\mathcal{L})}. \tag{6}$$

3. UAV Dynamics and the Von Karman Wind Model

In this section, the mathematical expressions that describe both rotorcraft and external disturbances in the form of turbulent wind are introduced. The Newton–Euler dynamics of the quadrotor contemplate an inertial reference frame (X_0, Y_0, Z_0) with origin at a point in the Earth and a body reference frame (X_1, Y_1, Z_1) with origin in the center of mass of the UAV (see Figure 1). Moreover, the angular dynamics is considered to be the same in both frames since we assume small roll and pitch rotations [46]. Then, the equations of motion of the aerial vehicle are defined as

$$\dot{\mathbf{d}} = \mathbf{R}\mathbf{v}, \tag{7}$$

$$m\dot{\mathbf{v}} = \mathbf{f} - m\boldsymbol{\omega} \times \mathbf{v}, \tag{8}$$

$$\mathbf{f} = -T_h\mathbf{e_3} + \mathbf{R}^{-1}mg\mathbf{e_3} + \mathbf{R}^{-1}\delta, \tag{9}$$

$$\dot{\boldsymbol{\Theta}} = \boldsymbol{\omega}, \tag{10}$$

$$\dot{\boldsymbol{\omega}} = \mathbf{J}^{-1}(\boldsymbol{\tau} - \boldsymbol{\omega} \times \mathbf{J}\boldsymbol{\omega}), \tag{11}$$

where $\mathbf{d} = [x, y, z]^T$ represents the inertial frame linear position of the UAV, $\mathbf{v} = [u, v, w]^T$ is the body frame linear velocity, $\boldsymbol{\Theta} = [\phi, \theta, \psi]^T$ is the attitude of the UAV, while $\boldsymbol{\omega}$ is its angular velocity; $\mathbf{R}$ is the body to inertial frame rotation matrix, vector $\mathbf{f}$ involves the linear forces that influence the quadrotor, $\delta = [\delta_x, \delta_y, \delta_z]^T$ describes the external disturbances that affect the quadrotor, T_h is the total thrust of the four motors, i.e., $T_h = T_{h1} + T_{h2} + T_{h3} + T_{h4}$, m is the mass of the aerial vehicle, g is the gravity acceleration, and $\mathbf{e_3} = [0, 0, 1]^T$ is a direction vector. Furthermore, assuming mechanical symmetry, the inertia matrix $\mathbf{J}$ is established as

$$\mathbf{J} = \begin{bmatrix} J_{xx} & 0 & 0 \\ 0 & J_{yy} & 0 \\ 0 & 0 & J_{zz} \end{bmatrix}. \tag{12}$$

Finally, the torques generated by the motors are defined in vector $\boldsymbol{\tau} = [\tau_\phi, \tau_\theta, \tau_\psi]^T$, where

$$\begin{bmatrix} \tau_\phi \\ \tau_\theta \\ \tau_\psi \end{bmatrix} = \begin{bmatrix} l\sin(\pi/4)(T_{h1} - T_{h2} - T_{h3} + T_{h4}) \\ l\sin(\pi/4)(T_{h1} + T_{h2} - T_{h3} - T_{h4}) \\ -\tau_1 + \tau_2 - \tau_3 + \tau_4 \end{bmatrix}, \tag{13}$$

with l as the distance from the center of each motor to the center of mass of the UAV, $\sin(\pi/4)$ as the angle between them, and T_{hi}, τ_i for $i = 1, 2, 3, 4$ as the thrust and torque from each motor, respectively, which can be expressed as

$$T_{hi} = C_T \Omega_i^2, \tag{14}$$

$$\tau_i = C_\tau \Omega_i^2. \tag{15}$$

with C_T as the thrust constant, C_τ as the moment constant, and Ω_i as the angular velocity of motor i. Now, assuming the existence of model uncertainties regarding the angular dynamics and the mass of the rotorcraft, the inertial frame equations of motion of the quadrotor are rewritten in the scalar form as

$$\ddot{\phi} = \frac{\tau_\phi}{J_{xx}}, \tag{16}$$

$$\ddot{\theta} = \frac{\tau_\theta}{J_{yy}}, \tag{17}$$

$$\ddot{\psi} = \frac{\tau_\psi}{J_{zz}}, \tag{18}$$

$$\ddot{x} = \frac{T_h}{m_u}(s_\phi s_\psi + c_\phi c_\psi s_\theta) + \frac{\delta_x(t)}{m_u}, \tag{19}$$

$$\ddot{y} = \frac{T_h}{m_u}(c_\phi s_\psi s_\theta + c_\psi s_\phi) + \frac{\delta_y(t)}{m_u}, \tag{20}$$

$$\ddot{z} = \frac{T_h}{m_u}(c_\phi c_\theta) + g + \frac{\delta_z(t)}{m_u}, \tag{21}$$

where m_u is a nominal value of m such that $m_u \approx m$ while $s_\star$ and $c_\star$ are the sine and cosine functions, respectively. External disturbance terms δ_x, δ_y, and δ_z are analyzed as drag forces due to turbulent wind through the following equation [23]:

$$\delta_* = -\frac{1}{2}\rho B_* A_* (\dot{d}_* - v_{w*})^2 \text{sign}(\dot{d}_* - v_{w*}), \tag{22}$$

where $* = \{x, y, z\}$, ρ is the air density, B is the drag coefficient in the inertial frame axis; A is the area of the quadrotor in each axis plane, and v_{w*} is the inertial frame wind velocity given by

$$\begin{aligned} v_{wx} &= \bar{v}_{wx} + \zeta_u, \\ v_{wy} &= \bar{v}_{wy} + \zeta_v, \\ v_{wz} &= \bar{v}_{wz} + \zeta_w, \end{aligned} \tag{23}$$

where $\bar{v}_{w*}$ is the inertial frame mean wind velocity while ζ_u, ζ_v and ζ_w are wind deviations described by the Von Karman wind turbulence model [47]:

$$\frac{\zeta_u(S)}{n_u(S)} = \frac{\eta_u\sqrt{\frac{2L_u}{\pi V}}(1+0.25\frac{L_u}{V}S)}{1+1.357\frac{L_u}{V}S+0.1987(\frac{L_u}{V})^2S^2}, \tag{24}$$

$$\frac{\zeta_v(S)}{n_v(S)} = \frac{\eta_v\sqrt{\frac{L_v}{\pi V}}(1+2.7478\frac{L_v}{V}S+0.3398(\frac{L_v}{V})^2S^2)}{1+2.9958\frac{L_v}{V}S+1.9754(\frac{L_v}{V})^2S^2+0.1539(\frac{L_v}{V})^3S^3}, \tag{25}$$

$$\frac{\zeta_w(S)}{n_w(S)} = \frac{\eta_w\sqrt{\frac{L_w}{\pi V}}(1+2.7478\frac{L_w}{V}S+0.3398(\frac{L_w}{V})^2S^2)}{1+2.9958\frac{L_w}{V}S+1.9754(\frac{L_w}{V})^2S^2+0.1539(\frac{L_w}{V})^3S^3}, \tag{26}$$

with white noise signals n_u, n_v, n_w and low-altitude parameters

$$L_w = z, \tag{27}$$

$$L_u = L_v = \frac{z}{(0.177+0.000823z)^{1.2}}, \tag{28}$$

and

$$\eta_w = 0.1W_{20}, \tag{29}$$

$$\eta_u = \eta_v = \frac{\eta_w}{(0.177+0.000823z)^{0.4}}, \tag{30}$$

where L_u, L_v, and L_w are turbulence scale lengths, and

$$V = \sqrt{(\dot{d}_x - v_{wx})^2 + (\dot{d}_y - v_{wy})^2 + (\dot{d}_z - v_{wz})^2}. \tag{31}$$

Terms η_u, η_v, and η_w depend on W_{20}, whose value denotes the wind velocity at an altitude of 6 m according to regulation MIL-HDBK-1797 [18] and specifies whether the turbulence intensity is light ($W_{20} = 15$ knots), moderate ($W_{20} = 30$ knots), or severe ($W_{20} = 45$ knots).

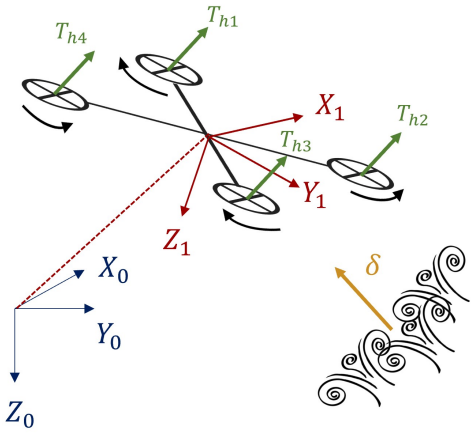

Figure 1. Quadrotor UAV. Reference frames.

4. FxtESO-Based ASMC Design

This section describes the design of a fixed-time extended state observer-based adaptive sliding mode strategy. The control objective is to drive a quadrotor UAV while tracking a desired trajectory in the presence of turbulent wind gusts. Assuming that the position measurements of the quadrotor are the only available states, the FxtESO supplies full-state and disturbance estimations within fixed-time convergence, whereas the ASMC drives the pose of the quadrotor while providing practical finite-time convergence of the state, robustness against bounded external disturbances and model uncertainties, and chattering attenuation. Then, the flight control scheme is composed of an inner loop that deals with the fast dynamics of the vehicle and an outer loop that handles the linear position of the UAV and the external disturbances rejection; see Figure 2.

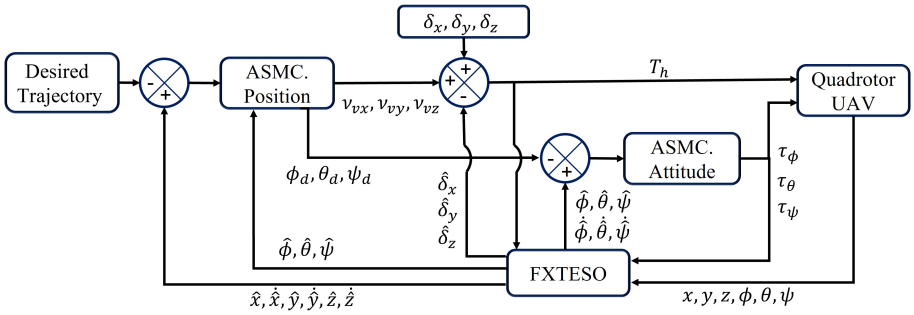

Figure 2. FxtESO−based ASMC scheme.

4.1. Fixed-Time Extended State Observer

We consider the following SISO nonlinear system:

$$\dot{\xi}_1 = \xi_2, \tag{32}$$
$$\dot{\xi}_2 = a(\xi) + b(\xi)u_r, \tag{33}$$
$$c = \xi_1, \tag{34}$$

where $\boldsymbol{\xi} = [\xi_1, \xi_2]^T$ denotes the state variables, u_r is the control input, c is the output of the system, and $a(\xi), b(\xi)$ are continuously differentiable functions. Now, extending to a third-order system, we have

$$\dot{\xi}_1 = \xi_2, \tag{35}$$
$$\dot{\xi}_2 = \xi_3 + \hat{b}(\xi)u_r, \tag{36}$$
$$\dot{\xi}_3 = \gamma(\boldsymbol{\xi}), \tag{37}$$
$$c = \xi_1, \tag{38}$$

where $|\hat{b}(\xi)| > 0$ is a bounded nominal model of $b(\xi)$, and $\xi_3 = \Delta\delta + \hat{a}(\xi)$ is a continuously differentiable and globally bounded augmented state that describes the total disturbance composed of those external perturbations and model uncertainties affecting the system. Finally, $|\gamma(\boldsymbol{\xi})| \geq 0$ denotes the dynamics of the extended state. Moreover, estimations of state variables ξ_1, ξ_2 and ξ_3 are given by FxtESO [48]:

$$\begin{aligned}
\dot{\hat{\xi}}_1 &= \hat{\xi}_2 + \kappa_1 \mathrm{sig}^{\alpha_1}(\tilde{\xi}) + \varepsilon_1 \mathrm{sig}^{\beta_1}(\tilde{\xi}), \\
\dot{\hat{\xi}}_2 &= \hat{\xi}_3 + \kappa_2 \mathrm{sig}^{\alpha_2}(\tilde{\xi}) + \varepsilon_2 \mathrm{sig}^{\beta_2}(\tilde{\xi}) + \hat{b}(\xi)u_r, \\
\dot{\hat{\xi}}_3 &= \kappa_3 \mathrm{sig}^{\alpha_3}(\tilde{\xi}) + \varepsilon_3 \mathrm{sig}^{\beta_3}(\tilde{\xi}) + \chi \mathrm{sign}(\tilde{\xi}),
\end{aligned} \tag{39}$$

with estimation error $\tilde{\xi} = \xi_1 - \hat{\xi}_1$, parameters $\kappa_1, \kappa_2, \kappa_3, \varepsilon_1, \varepsilon_2, \varepsilon_3 \in \mathbb{R}^+$, and $\chi > |\gamma(\xi)|$. Considering a small enough scalar φ_1, parameters $\alpha_{1,2,3}$ are defined as $\alpha_1 \in (1 - \varphi_1, 1)$, $\alpha_2 = 2\alpha_1 - 1$, and $\alpha_3 = 3\alpha_1 - 2$. In that sense, by choosing φ_2 to be sufficiently small, terms $\beta_{1,2,3}$ are established as $\beta_1 \in (1, 1 + \varphi_2)$, $\beta_2 = 2\beta_1 - 1$, and $\beta_3 = 3\beta_1 - 2$. Furthermore, by taking Equation (36), the control law of the augmented system yields

$$u_r = \frac{-\hat{\xi}_3 + \nu_a}{\hat{b}(\hat{\xi})}, \tag{40}$$

with ν_a as an auxiliary control strategy designed to control the positioning and orientation of the quadrotor UAV.

4.2. Attitude Controller

In order to design a controller for the rotational motion, the angular dynamics equations of the quadrotor are rewritten as

$$\dot{\boldsymbol{\omega}} = \mathbf{a}(\boldsymbol{\omega}) + \mathbf{b}(\boldsymbol{\omega})\boldsymbol{\tau}, \tag{41}$$

$$\mathbf{c_a} = \boldsymbol{\varsigma_a}(\boldsymbol{\omega})\boldsymbol{\omega}, \tag{42}$$

with states vector $\boldsymbol{\omega} = [\phi, \dot{\phi}, \theta, \dot{\theta}, \psi, \dot{\psi}]^T$, control input $\boldsymbol{\tau} = [\tau_\phi, \tau_\theta, \tau_\psi]^T$, $\boldsymbol{\varsigma_a}(\boldsymbol{\omega}) \in \mathbb{R}^{3\times 6}$, and $\mathbf{c_a} = [\phi, \theta, \psi]^T$ as the available state. Introducing the desired states $\boldsymbol{\omega_d} = [\phi_d, \dot{\phi}_d, \theta_d, \dot{\theta}_d, \psi_d, \dot{\psi}_d]^T$ and the error vector $\mathbf{e_a} = [\phi - \phi_d, \theta - \theta_d, \psi - \psi_d]^T$, a sliding surface vector is designed as

$$\boldsymbol{\sigma_\omega} = \boldsymbol{\lambda_a}\mathbf{e_a} + \dot{\mathbf{e}}_\mathbf{a}, \tag{43}$$

with $\boldsymbol{\lambda_a} = \mathrm{diag}(\lambda_\phi, \lambda_\theta, \lambda_\psi)$ and $\lambda_{\phi,\theta,\psi} > 0$. Then, the changing rate of (43) yields

$$\dot{\boldsymbol{\sigma}}_\omega = \boldsymbol{\lambda_a}\dot{\mathbf{e}}_\mathbf{a} + \ddot{\mathbf{e}}_\mathbf{a}. \tag{44}$$

Equations (16)–(18) are substituted in (44) to perform a feedback linearization in the form of (40) as follows [49]:

$$\begin{bmatrix} \tau_\phi \\ \tau_\theta \\ \tau_\psi \end{bmatrix} = \begin{bmatrix} J_{xx}(-\lambda_\phi(\dot{\phi} - \dot{\phi}_d) + \ddot{\phi}_d - \hat{\xi}_{3,\phi} + \nu_\phi \\ J_{yy}(-\lambda_\theta(\dot{\theta} - \dot{\theta}_d) + \ddot{\theta}_d - \hat{\xi}_{3,\theta} + \nu_\theta \\ J_{zz}(-\lambda_\psi(\dot{\psi} - \dot{\psi}_d) + \ddot{\psi}_d - \hat{\xi}_{3,\psi} + \nu_\psi \end{bmatrix}, \tag{45}$$

where $\hat{\xi}_{3,\phi}$, $\hat{\xi}_{3,\theta}$, and $\hat{\xi}_{3,\psi}$ are the total disturbance estimates for the attitude subsystem while ν_ϕ, ν_θ and ν_ψ are auxiliary controllers described by the adaptive sliding mode strategy

$$\nu_\dagger = -K_{1\dagger}(t)\mathrm{sig}^{1/2}(\sigma_\dagger) - K_{2\dagger}\sigma_\dagger, \tag{46}$$

with $\dagger = \{\phi, \theta, \psi\}$, $K_{2\dagger} > 0$, and $K_{1\dagger}$ as the adaptive gain with adaptability law

$$\dot{K}_{1\dagger}(t) = \begin{cases} k_\dagger \mathrm{sign}(|\sigma_\dagger| - \mu_\dagger) & K_{1\dagger} > k_{\min\dagger} \\ k_{\min\dagger} & K_{1\dagger} \leq k_{\min\dagger} \end{cases}, \tag{47}$$

where $k > 0$ is the adaptation rate regulator, $\mu > 0$ is the adaptiveness threshold, and $k_{\min} \in \mathbb{R}^+$ ensures the delivery of the lowest control effort to the system. Then, $K_{1\dagger}$ increases its magnitude when condition $|\sigma| > \mu$ is met. On the other hand, once $|\sigma| \leq \mu$ is true, the adaptive gain starts decreasing until achieving the value of $k_{\min}$. Moreover, the chattering attenuation property of the ASMC can be attributed to two factors: first, structure $\mathrm{sig}^{1/2}(\cdot)$ guarantees smooth and continuous responses from (46), and second the non-overestimation of gain $K_{1\dagger}$ due to its designed dynamics (47).

4.3. Positioning Controller

We consider the translation dynamics of the quadrotor as

$$\dot{\boldsymbol{\varrho}} = \mathbf{a_p}(\boldsymbol{\varrho}) + \mathbf{b_p}(\boldsymbol{\varrho})T_h + \mathbf{o}(t), \tag{48}$$

$$\mathbf{c_p} = \boldsymbol{\varsigma_p}(\boldsymbol{\varrho})\boldsymbol{\varrho}, \tag{49}$$

with state vector $\boldsymbol{\varrho} = [x, \dot{x}, y, \dot{y}, z, \dot{z}]^T$, control input T_h, which is equivalent to the total propulsion force of the motors, $\mathbf{o}(t) = 1/m[0, \delta_x(t), 0, \delta_y(t), 0, \delta_z(t)]^T$ as the external disturbances vector, $\boldsymbol{\varsigma_p}(\boldsymbol{\omega}) \in \mathbb{R}^{3\times 6}$, and $\mathbf{c_p} = [x, y, z]^T$ as the available state. Moving on, the desired linear state and the position error vectors are, respectively, defined as $\boldsymbol{\varrho_d} = [x_d, \dot{x}_d, y_d, \dot{y}_d, z_d, \dot{z}_d]^T$ and $\mathbf{e_p} = [x - x_d, y - y_d, z - z_d]^T$. Hence, the sliding surface is established as

$$\sigma_\rho = \boldsymbol{\lambda}_p \mathbf{e_p} + \dot{\mathbf{e}}_\mathbf{p}, \tag{50}$$

where $\boldsymbol{\lambda_p} = \text{diag}(\lambda_x, \lambda_y, \lambda_z)$ and $\lambda_{x,y,z} > 0$. Thus,

$$\dot{\sigma}_\rho = \boldsymbol{\lambda}_p \dot{\mathbf{e}}_\mathbf{p} + \ddot{\mathbf{e}}_\mathbf{p}. \tag{51}$$

Since the translation dynamics of the quadrotor are underactuated, feedback linearization cannot be performed directly after substituting (19)–(21) in (51). Therefore, the following virtual auxiliary control strategy is adopted:

$$\begin{bmatrix} \nu_{vx} \\ \nu_{vy} \\ \nu_{vz} \end{bmatrix} = \begin{bmatrix} (T_h/m_u)(s_{\hat{\phi}} s_{\hat{\psi}} + c_{\hat{\phi}} c_{\hat{\psi}} s_{\hat{\theta}}) \\ (T_h/m_u)(c_{\hat{\phi}} s_{\hat{\psi}} s_{\hat{\theta}} + c_{\hat{\psi}} s_{\hat{\phi}}) \\ (T_h/m_u)(c_{\hat{\phi}} c_{\hat{\theta}}) \end{bmatrix}. \tag{52}$$

Recalling that $* = \{x, y, z\}$, virtual controller ν_{v*} is described by the following ASMC with disturbance compensation:

$$\nu_{v*} = -K_{1*}(t)\text{sig}^{1/2}(\sigma_*) - K_{2*}\sigma_* - \hat{\xi}_{3,*}, \tag{53}$$

where the adaptability of K_{1*} was previously defined in (47), and $\hat{\xi}_{3,*}$ is the total disturbance estimation provided by FxtESO. Additionally, to fulfill the desired x and y trajectories, the desired roll and pitch rotations are determined by

$$\theta_d = \text{asin}\left(\frac{(m_u/T_h)\nu_{vx} - s_{\psi_d} s_{\phi_d})}{c_{\psi_d} c_{\phi_d}} \right), \tag{54}$$

$$\phi_d = \text{asin}\left((m_u/T_h)(s_{\psi_d}\nu_{vx} - c_{\psi_d}\nu_{vy}) \right). \tag{55}$$

Next, the z-dynamics are stabilized by control input T_h as

$$T_h = \frac{m_u}{c_{\hat{\phi}} c_{\hat{\theta}}} \left(\nu_{vz} - \hat{\xi}_{3,z} + \ddot{z}_d - \lambda_z(\dot{\hat{z}} - \dot{z}_d) \right). \tag{56}$$

4.4. Stability Analysis

The stability analysis of the extended state observer-based adaptive controller is addressed. Then, the following Theorem is stated:

Theorem 1. *The sliding mode controller (46) with adaptive gain dynamics (47) using the fixed-time estimations from (39) in a closed loop with a nonlinear system (7)–(11) offers a practical finite-time convergence of the state error at bounded time $t \leq T_k(\sigma_0)$.*

Proof. In order to provide the stability, we have consider three stages:

FxtESO Convergence Analysis

We consider estimation errors

$$\tilde{\xi}_i = \xi_i - \hat{\xi}_i, \text{ for } i = \{1, 2, 3\} \tag{57}$$

with time-derivative

$$\begin{aligned} \dot{\tilde{\xi}}_1 &= \tilde{\xi}_2 - \kappa_1 \text{sig}^{\alpha_1}(\tilde{\xi}_1) - \varepsilon_1 \text{sig}^{\beta_1}(\tilde{\xi}_1), \\ \dot{\tilde{\xi}}_2 &= \tilde{\xi}_3 - \kappa_2 \text{sig}^{\alpha_2}(\tilde{\xi}_1) - \varepsilon_2 \text{sig}^{\beta_2}(\tilde{\xi}_1), \\ \dot{\tilde{\xi}}_3 &= \gamma(\boldsymbol{\xi}) - \kappa_3 \text{sig}^{\alpha_3}(\tilde{\xi}_1) - \varepsilon_3 \text{sig}^{\beta_3}(\tilde{\xi}_1) - \chi \text{sign}(\tilde{\xi}_1). \end{aligned} \tag{58}$$

Then, to prove the fixed-time convergence of the observer, the analysis of the estimation error dynamics (58) is divided into two sections [50]. First, we consider subsystem

$$\begin{aligned}\dot{\tilde{\xi}}_1 &= \tilde{\xi}_2 - \kappa_1 \mathrm{sig}^{\alpha_1}(\tilde{\xi}_1),\\ \dot{\tilde{\xi}}_2 &= \tilde{\xi}_3 - \kappa_2 \mathrm{sig}^{\alpha_2}(\tilde{\xi}_1),\\ \dot{\tilde{\xi}}_3 &= -\kappa_3 \mathrm{sig}^{\alpha_3}(\tilde{\xi}_1),\end{aligned} \tag{59}$$

and terms

$$\mathbf{K} = \begin{bmatrix} -\kappa_1 & 1 & 0\\ -\kappa_2 & 0 & 1\\ -\kappa_3 & 0 & 0\end{bmatrix}; \quad \tilde{\boldsymbol{\xi}}_{\boldsymbol{\alpha}} = [\tilde{\xi}_1^{\frac{1}{\varrho_1}}, \tilde{\xi}_2^{\frac{1}{\varrho_2}}, \tilde{\xi}_3^{\frac{1}{\varrho_3}}]^T, \tag{60}$$

with $\varrho_i = (i-1)\bar{\alpha} - (i-2)$ for $i = 1, 2, 3$. Referring to the work from Perruquetti et al. [43], system $\dot{\tilde{\boldsymbol{\xi}}}_{\boldsymbol{\alpha}} = \mathbf{K}\tilde{\boldsymbol{\xi}}_{\boldsymbol{\alpha}}$ is achievable by choosing $\bar{\alpha} = 1$. Since $\mathbf{K}$ is Hurwitz, $\dot{\tilde{\boldsymbol{\xi}}}_{\boldsymbol{\alpha}}$ is asymptotically stable. Then, there is a Lyapunov function $V(\tilde{\boldsymbol{\xi}}_{\boldsymbol{\alpha}}) = \tilde{\boldsymbol{\xi}}_{\boldsymbol{\alpha}}{}^T \mathbf{P} \tilde{\boldsymbol{\xi}}_{\boldsymbol{\alpha}}$ that fulfills the following:

1. Matrix $\mathbf{P}$ is the solution of Lyapunov equation $\mathbf{K}^T\mathbf{P} + \mathbf{P}\mathbf{K} = -\mathbf{I}$ with identity matrix $\mathbf{I} \in \mathbb{R}^{3\times 3}$.
2.

$$\begin{aligned}\dot{V}(\tilde{\boldsymbol{x}}_{\boldsymbol{\alpha}}) &= \dot{\tilde{\boldsymbol{\xi}}}_{\boldsymbol{\alpha}}{}^T \mathbf{P} \tilde{\boldsymbol{\xi}}_{\boldsymbol{\alpha}} + \tilde{\boldsymbol{\xi}}_{\boldsymbol{\alpha}}{}^T \mathbf{P} \dot{\tilde{\boldsymbol{\xi}}}_{\boldsymbol{\alpha}}\\ &= \tilde{\boldsymbol{\xi}}_{\boldsymbol{\alpha}}{}^T \mathbf{K}^T \mathbf{P} + \tilde{\boldsymbol{\xi}}_{\boldsymbol{\alpha}}{}^T \mathbf{P}\mathbf{K} \tilde{\boldsymbol{\xi}}_{\boldsymbol{\alpha}}\\ &= \tilde{\boldsymbol{\xi}}_{\boldsymbol{\alpha}}{}^T (\mathbf{K}^T\mathbf{P} + \mathbf{P}\mathbf{K}) \tilde{\boldsymbol{\xi}}_{\boldsymbol{\alpha}}\\ &= -\tilde{\boldsymbol{\xi}}_{\boldsymbol{\alpha}}{}^T \mathbf{I} \tilde{\boldsymbol{\xi}}_{\boldsymbol{\alpha}} < 0.\end{aligned} \tag{61}$$

Moreover, Equation (61) is also valid for $\bar{\alpha} \in (1-\varphi_1, 1)$, $0 < \varphi_1 < 1$ [51]. Thus, $V(\tilde{\boldsymbol{\xi}}_{\boldsymbol{\alpha}})$ is a Lyapunov candidate function for error Subsystem (59). In addition, according to Lemma 1, (59) is a homogeneous system of degree $\bar{\alpha} - 1 < 0$. Consequently, Lemma 2 holds for this case and

$$\dot{V}(\tilde{\boldsymbol{\xi}}_{\boldsymbol{\alpha}}) = -\varsigma_\alpha V^{\iota_1}(\tilde{\boldsymbol{\xi}}_{\boldsymbol{\alpha}}), \tag{62}$$

where $\varsigma_\alpha > 0$ and $0 < \iota_1 < 1$. Now, we consider the second half of (58):

$$\begin{aligned}\dot{\tilde{\xi}}_1 &= \tilde{\xi}_2 - \varepsilon_1 \mathrm{sig}^{\beta 1}(\tilde{\xi}_1),\\ \dot{\tilde{\xi}}_2 &= \tilde{\xi}_3 - \varepsilon_2 \mathrm{sig}^{\beta 2}(\tilde{\xi}_1),\\ \dot{\tilde{\xi}}_3 &= -\varepsilon_3 \mathrm{sig}^{\beta 3}(\tilde{\xi}_1),\end{aligned} \tag{63}$$

and we let

$$\mathbf{E} = \begin{bmatrix} -\varepsilon_1 & 1 & 0\\ -\varepsilon_2 & 0 & 1\\ -\varepsilon_3 & 0 & 0\end{bmatrix}; \quad \tilde{\boldsymbol{\xi}}_{\boldsymbol{\beta}} = [\tilde{\xi}_1^{\frac{1}{\upsilon_1}}, \tilde{\xi}_2^{\frac{1}{\upsilon_2}}, \tilde{\xi}_3^{\frac{1}{\upsilon_3}}]^T, \tag{64}$$

with $\upsilon_j = (j-1)\bar{\beta} - (j-2)$ for $j = 1, 2, 3$. Similarly to the previous analysis, if $\bar{\beta} = 1$, system $\dot{\tilde{\boldsymbol{\xi}}}_{\boldsymbol{\beta}} = \mathbf{E}\tilde{\boldsymbol{\xi}}_{\boldsymbol{\beta}}$ is asymptotically stable. Thus, there is a Lyapunov function $V_a(\tilde{\boldsymbol{\xi}}_{\boldsymbol{\beta}}) = \tilde{\boldsymbol{\xi}}_{\boldsymbol{\beta}}^T \mathbf{P}_\mathbf{a} \tilde{\boldsymbol{\xi}}_{\boldsymbol{\beta}}$ with derivative $\dot{V}_a(\tilde{\boldsymbol{\xi}}_{\boldsymbol{\beta}}) = -\tilde{\boldsymbol{\xi}}_{\boldsymbol{\beta}}^T \mathbf{I} \tilde{\boldsymbol{\xi}}_{\boldsymbol{\beta}} < 0$, which also holds when $\bar{\beta} \in (1, 1+\varphi_2)$ with small enough φ_2. By means of Lemma 1, Subsystem (63) is homogeneous of degree $\bar{\beta} - 1 > 0$. Furthermore, referring to Basin et al. [51], the subsystem can be written in the form

$$\dot{V}(\tilde{\boldsymbol{\xi}}_{\boldsymbol{\beta}}) = -\varsigma_\beta V_a^{\iota_2}(\tilde{\boldsymbol{\xi}}_{\boldsymbol{\beta}}), \tag{65}$$

with $\varsigma_\beta > 0$ and $\iota_2 > 1$. Hence, there is Lyapunov function $V_b(\tilde{\boldsymbol{\xi}})$ for error System (58) with derivative $\dot{V}_b(\tilde{\boldsymbol{\xi}}) = -(\varsigma_\alpha V_b^{\iota_1}(\tilde{\boldsymbol{\xi}}) + \varsigma_\beta V_b^{\iota_2}(\tilde{\boldsymbol{\xi}}))$. Then, according to Lemma 3, observer error $\tilde{\boldsymbol{\xi}} = [\tilde{\xi}_1, \tilde{\xi}_2, \tilde{\xi}_3]^T$ converges to zero in a fixed time defined by [52]

$$T_f \leq \frac{\lambda_{\max}^{1-\bar{\alpha}}(\mathbf{P})}{\varsigma_\alpha(1-\bar{\alpha})} + \frac{1}{\varsigma_\beta(\beta-1)\lambda_{\min}(\mathbf{P_a})^{\beta-1}}, \tag{66}$$

where $\lambda_{\max}(\mathbf{P})$ is the maximum eigenvalue of $\mathbf{P}$, and $\lambda_{\min}(\mathbf{P_a})$ is the minimum eigenvalue of $\mathbf{P_a}$. Moreover, since $\tilde{\xi}_1, \dot{\tilde{\xi}}_1 \to 0$ as $t \to T_f$, $\tilde{\xi}_2$ and $\tilde{\xi}_3$ also tend to zero. Then, $\tilde{\boldsymbol{\xi}} = 0$ when $t > T_f$, which means that the equivalent control identity given by

$$\dot{\tilde{\xi}}_3 = \gamma(\boldsymbol{\xi}) - \chi sign(\tilde{\xi}_1) = 0 \tag{67}$$

holds [53]. We notice that $\tilde{\xi}_3 = 0$ cannot be accomplished in practice due to several factors such as noise conditions, sampling frequency, and the disturbance dynamics [50]. However, assuming bounded perturbations and uncertainties, the fixed-time attractiveness of (39) allows the reaching of a small vicinity $\varkappa > 0$ such that $\tilde{\xi}_3 \in \varkappa$, after $t > T_f$.

Adaptive Sliding Mode Control Stability

By taking Equations (40), (44), and (51), the closed-loop FxtESO-based ASMC system, in a single-input single-output form, is expressed as

$$\dot{\sigma} = -K_1(t)\text{sig}^{1/2}(\sigma) - K_2\sigma + \tilde{\xi}_3, \tag{68}$$

recalling that $\tilde{\xi}_3 = \xi_3 - \hat{\xi}_3$ represents the estimation error for the total disturbance. Then, the Lyapunov candidate function for the stability analysis of the system is selected as [54]

$$V(\sigma) = \frac{1}{2}\sigma^2 + \frac{1}{2}(K_1(t) - K_{\mathcal{M}})^2, \tag{69}$$

where $K_{\mathcal{M}}$ is a value of adaptive gain K_1 that satisfies inequality $(K_1(t) - K_{\mathcal{M}}) < 0$ and [49]

$$K_{\mathcal{M}}(t) > \frac{1}{|\sigma|^{\frac{1}{2}}}(\delta_{max} - K_2|\sigma|), \tag{70}$$

$$0 < |\xi_3| \leq \delta_{max}. \tag{71}$$

While condition $K_1(t) > K_{min}$ holds, the time differentiation of (69) is

$$\dot{V}(\sigma) = \sigma\dot{\sigma} + (K_1(t) - K_{\mathcal{M}})(k\ \text{sign}(|\sigma| - \mu)). \tag{72}$$

By substituting (68) and (71) in (72),

$$\begin{aligned}\dot{V}(\sigma) \leq |\sigma|(&-K_1(t)|\sigma|^{\frac{1}{2}}\text{sign}(\sigma) - K_2\sigma \\ &+ \delta_{max}) + (K_1(t) - K_{\mathcal{M}})(k\ \text{sign}(|\sigma| - \mu)).\end{aligned} \tag{73}$$

Now, terms $\pm K_{\mathcal{M}}|\sigma|^{\frac{3}{2}}$ are introduced and applied as follows:

$$\begin{aligned}\dot{V}(\sigma) \leq |\sigma|(&-K_{\mathcal{M}}|\sigma|^{\frac{1}{2}} - K_2|\sigma| + \delta_{max}) \\ &+ (K_1(t) - K_{\mathcal{M}})(k\ \text{sign}(|\sigma| - \mu) - |\sigma|^{\frac{3}{2}})\end{aligned}. \tag{74}$$

For the sake of simplicity, we let $h_p = K_{\mathcal{M}}|\sigma|^{\frac{1}{2}} + K_2|\sigma| - \delta_{max} \in \mathbb{R}^+$. Then, (74) yields

$$\dot{V}(\sigma) \leq -h_p|\sigma| + (K_1(t) - K_{\mathcal{M}})(k\ \text{sign}(|\sigma| - \mu) - |\sigma|^{\frac{3}{2}}). \tag{75}$$

Then, the new terms $\pm h_q|K_1(t) - K_{\mathcal{M}}|$ with $|K_1(t) - K_{\mathcal{M}}| = -(K_1(t) - K_{\mathcal{M}})$ and $h_q > 0$ are added up in (75), which results in

$$\begin{aligned}\dot{V}(\sigma) &\leq -h_p|\sigma| - h_q|K_1(t) - K_{\mathcal{M}}| \\ &+ |K_1(t) - K_{\mathcal{M}}|(h_q - k\,\mathrm{sign}(|\sigma| - \mu) + |\sigma|^{\frac{3}{2}}) \\ &\leq -h_p\frac{\sqrt{2}}{\sqrt{2}}|\sigma| - h_q\frac{\sqrt{2}}{\sqrt{2}}|K1(t) - K_{\mathcal{M}}| \\ &+ |K_1(t) - K_{\mathcal{M}}|(h_q - k\,\mathrm{sign}(|\sigma| - \mu) + |\sigma|^{\frac{3}{2}}) \\ &\leq -\min\{h_p\sqrt{2}, h_q\sqrt{2}\}\left(\frac{|\sigma|}{\sqrt{2}} + \frac{|K_1(t) - K_{\mathcal{M}}|}{\sqrt{2}}\right) \\ &+ |K_1(t) - K_{\mathcal{M}}|(h_q - k\,\mathrm{sign}(|\sigma| - \mu) + |\sigma|^{\frac{3}{2}}).\end{aligned} \tag{76}$$

The previous equation can be rewritten in the form of (4) from Lemma 4 with $h = \min\{h_p\sqrt{2}, h_q\sqrt{2}\}$, $\mathcal{L} = 0.5$ and $\mathcal{W} = |K_1(t) - K_{\mathcal{M}}|(h_q - k\,\mathrm{sign}(|\sigma| - \mu) + |\sigma|^{\frac{3}{2}}) > 0$. Therefore, referring to Definition 3, there is a small neighborhood of zero described by $\Gamma > 0$ such that the achievement of the sliding mode in a practical finite-time can be divided into two phases: (1) the reaching phase when $|\sigma| > \Gamma$ and (2) the controller convergence when $|\sigma| \leq \Gamma$ at time

$$T_k \leq \frac{V^{\frac{1}{2}}(\sigma_0)}{0.5\,\min\{h_p\sqrt{2}, h_q\sqrt{2}\}\mathcal{Y}_0}. \tag{77}$$

FxtESO-Based ASMC Stability

The previously proven fixed-time convergence of FxtESO and the practical finite-time convergence of the ASMC permit the separation principle to be fulfilled. Hence, both algorithms, controller and observer, can be designed independently [55]. Then, to avoid ambiguities, the gains of the extended observer, and thus its dynamics, are chosen such that the estimated states converge to the actual state at time T_f sufficiently faster than controller convergence T_k, i.e., $T_f \ll T_k$. The aforementioned is guaranteed as long as the total disturbance affecting the system remains in bounds $|\xi_3| \leq \delta_{\max}$. Thus, strong enough uncertainties and external disturbances, or long delays in the input or output, still can make the system unstable. The proof is complete. □

5. Results

The performance of the proposed observer-based control strategy was verified through computer simulations in the Matlab/Simulink environment. The 60 s virtual experiment was run at a frequency of 100 Hz and consisted of a quadrotor UAV executing a stationary flight followed by a spiral trajectory defined by

$$\begin{aligned}x_d(t) &= \begin{cases}0 & \text{if } 0 \leq t \leq 5 \\ -\int \sin 0.3(t-5)dt & \text{if } 5 < t \leq 60\end{cases}, \\ y_d(t) &= \begin{cases}0 & \text{if } 0 \leq t \leq 5 \\ \int \cos 0.3(t-5)dt & \text{if } 5 < t \leq 60\end{cases}, \\ z_d(t) &= \begin{cases}-2 & \text{if } 0 \leq t \leq 10 \\ -2 - 0.1(t-10) & \text{if } 10 < t \leq 60\end{cases}, \\ \psi_d(t) &= \begin{cases}0 & \text{if } 0 \leq t \leq 5 \\ 0.3(t-5) & \text{if } 5 < t \leq 60\end{cases}.\end{aligned} \tag{78}$$

The rotorcraft was completely exposed to severe turbulent wind fields described by the Von Karman model with parameters $\bar{v}_{wx} = -8$ m/s, $\bar{v}_{wy} = 10$ m/s, $\bar{v}_{wz} = 6$ m/s, $W_{20} = 45$ knots $= 23.15$ m/s, and $\rho = 1.2$ kg/m^3, where the resultant disturbances

can be appreciated in Figure 3. The quadrotor was programmed with initial conditions $\mathbf{d}(0) = [0,0,0]^T$ m, $\mathbf{\Theta}(0) = [0,0,0]^T$ rad, and specifications $J_{xx} = 0.0411$ kgm^2, $J_{yy} = 0.0478$ kgm^2, $J_{zz} = 0.0599$ kgm^2, $l = 0.225$ m, $K_T = 1.356 \times 10^{-5}$ N/(rad^2/s^2), $K_\tau = 2.036 \times 10^{-7}$ Nm/(rad^2/s^2), $B_x = B_y = 0.3$, $B_z = 0.5$, $A_x = A_y = 0.1$ m^2, and $A_z = 0.2$ m^2. Moreover, the vehicle was set with a mass of $m = 2$ kg. However, an approximate mass of $m_u = 1.75$ kg was included in the observer-based controller to show its effectiveness under model uncertainties. Additionally, white Gaussian noise signals of a 100 Hz frequency were applied to the outputs of the quadrotor. These signals are illustrated in Figure 4 and were established with mean 0.005 and standard deviation 0.001 for position measurements and mean 0.001 and standard deviation 0.001 for attitude measurements. Finally, the maximum motor thrust input was bounded to $-30 \leq T_h < 0$ N for design purposes. The chosen tuning parameters of the ASMC were $\lambda_x = \lambda_y = 1$, $\lambda_z = 2$, $K_{2x} = K_{2y} = 1$, $K_{2z} = 2$, $k_x = 0.2, k_y = 0.3, k_z = 0.5$, $\mu_x = \mu_y = \mu_z = 0.05, k_{min_x} = k_{min_y} = k_{min_z} = 0.01$ for the position subsystem, and $\lambda_\phi = \lambda_\theta = 8$, $\lambda_\psi = 2$, $K_{2\phi} = K_{2\theta} = 6$, $K_{2\psi} = 0.1$, $k_\phi = k_\theta = 0.5, k_\psi = 0.3$, $\mu_\phi = \mu_\theta = \mu_\psi = 0.05$, $k_{min_\phi} = k_{min_\theta} = 0.1$, and $k_{min_\psi} = 0.01$ for the attitude subsystem. To demonstrate that FxtESO with gains $\kappa_{1_{x,y,z,}} = \kappa_{1_{\phi,\theta,\psi}} = \varepsilon_{1_{x,y,z}} = \varepsilon_{1_{\phi,\theta,\psi}} = 10$, $\kappa_{2_{x,y,z,}} = \kappa_{2_{\phi,\theta,\psi}} = \varepsilon_{2_{x,y,z}} = \varepsilon_{2_{\phi,\theta,\psi}} = 25$, $\kappa_{3_{x,y,z,}} = \kappa_{3_{\phi,\theta,\psi}} = \varepsilon_{3_{x,y,z}} = \varepsilon_{3_{\phi,\theta,\psi}} = 25$, $\alpha_{1_{x,y,z}} = \alpha_{1_{\phi,\theta,\psi}} = 0.75$, $\alpha_{2_{x,y,z}} = \alpha_{2_{\phi,\theta,\psi}} = 0.4$, $\alpha_{3_{x,y,z}} = \alpha_{3_{\phi,\theta,\psi}} = 0.1$, $\beta_{1_{x,y,z}} = \beta_{1_{\phi,\theta,\psi}} = 1.2$, $\beta_{2_{x,y,z}} = \beta_{2_{\phi,\theta,\psi}} = 1.4$, $\beta_{3_{x,y,z}} = \beta_{3_{\phi,\theta,\psi}} = 1.6$, $\chi_{x,y,z} = \chi_{\phi,\theta,\psi} = 0.1$ recovers the target system, its initial conditions were set as $\hat{\mathbf{d}}(0) = [0,0,-0.1]^T$ m, and $\hat{\mathbf{\Theta}}(0) = [0.05, 0.05, 0.1]^T$ rad.

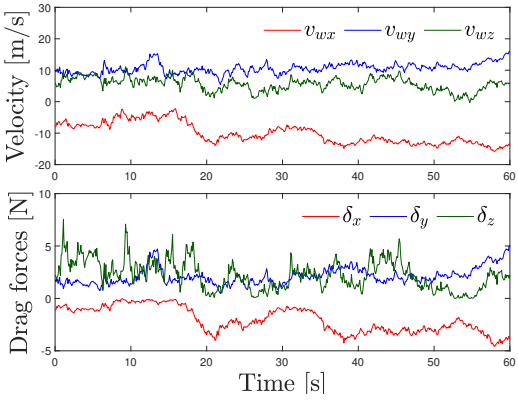

Figure 3. Resultant external disturbances described by the Von Karman wind model.

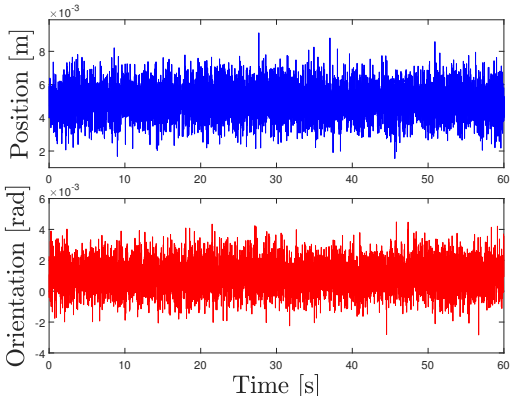

Figure 4. Applied sensor noise to the position and attitude measurements.

5.1. Disturbance Compensation

A comparison involving the FxtESO-based ASMC with (*w/DC*) and without (*w/o DC*) disturbance compensation was given to demonstrate the advantages of its implementation on the performance of the UAV. The applied turbulent wind gusts reached peak velocities of $\max(|v_{wx}|) = 15.83$ m/s, $\max(|v_{wy}|) = 16$ m/s, and $\max(|v_{wz}|) = 11.10$ m/s

which implied maximum drag forces of $\max(|\delta_x|) = 4.58$ N, $\max(|\delta_y|) = 5.03$ N, and $\max(|\delta_z|) = 7.51$ N. The latter is equivalent to 23.36%, 25.65%, and 38.30% of the total weight of the aerial vehicle. The execution of the trajectory of the rotorcraft, from a top view, is portrayed in Figure 5a. It is evident that the approach including the disturbance compensation action offered a superior tracking performance with slighter oscillations and deviations from the desired position. In addition, Figure 5b,c demonstrate two important differences among executions in the x and y axes. First, the disturbance rejection-based control system presented a more robust reaction to perturbations within the first seconds of the simulation, during the hover flight execution. Second, we note that it took longer for the feedback regulation-based sliding mode strategy to become close to the desired state due to the existence of both external disruptions and model uncertainties. Moving on, the vertical performance of the UAV is given in Figure 5d. The vehicle managed through the ASMC without disturbance compensation struggled in achieving the reference altitude at $t \leq 10$ since the turbulent wind fields were continuously pushing the quadrotor down. After $t \geq 10$, the discrepancies between both controllers were less perceptible. However, the zoomed-in section of the graph denotes slight oscillations on the obtained trajectory without disturbance compensation.

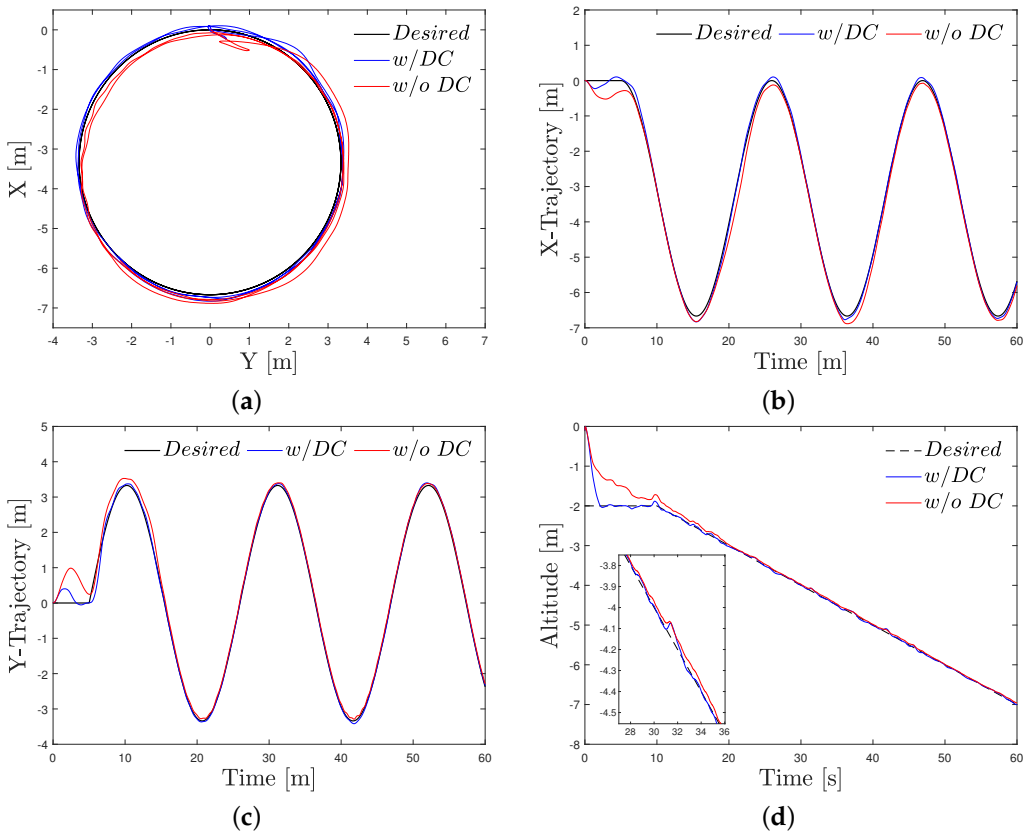

Figure 5. Disturbance compensation analysis. Trajectory tracking performance of (**a**) Top view, (**b**) y response, (**c**) x coordinate and (**d**) z axis evolution.

The heading performance of the UAV is displayed in Figure 6a. In this particular case, both controllers delivered a similar execution throughout the simulation except at interval $40 \leq t \leq 50$ where the disturbance compensation-free ASMC response presented slight oscillations. The executed roll and pitch rotations of the rotorcraft are shown in Figure 6b. During the time interval $0 < t < 20$, it is visible that the outputs from the proposed approach were smoother than those from the controller without disturbance compensation. This is expected since the disturbance compensation action demands faster responses from the system. Furthermore, we notice that once $t \geq 20$, unlike FxtESO-ASMC, the classic ASMC strategy began to occasionally provide high-frequency rotations. The latter suggests

that the vehicle was exposed to strong disturbances whose magnitude may be close to the maximum boundary it can handle without reaching an unstable state.

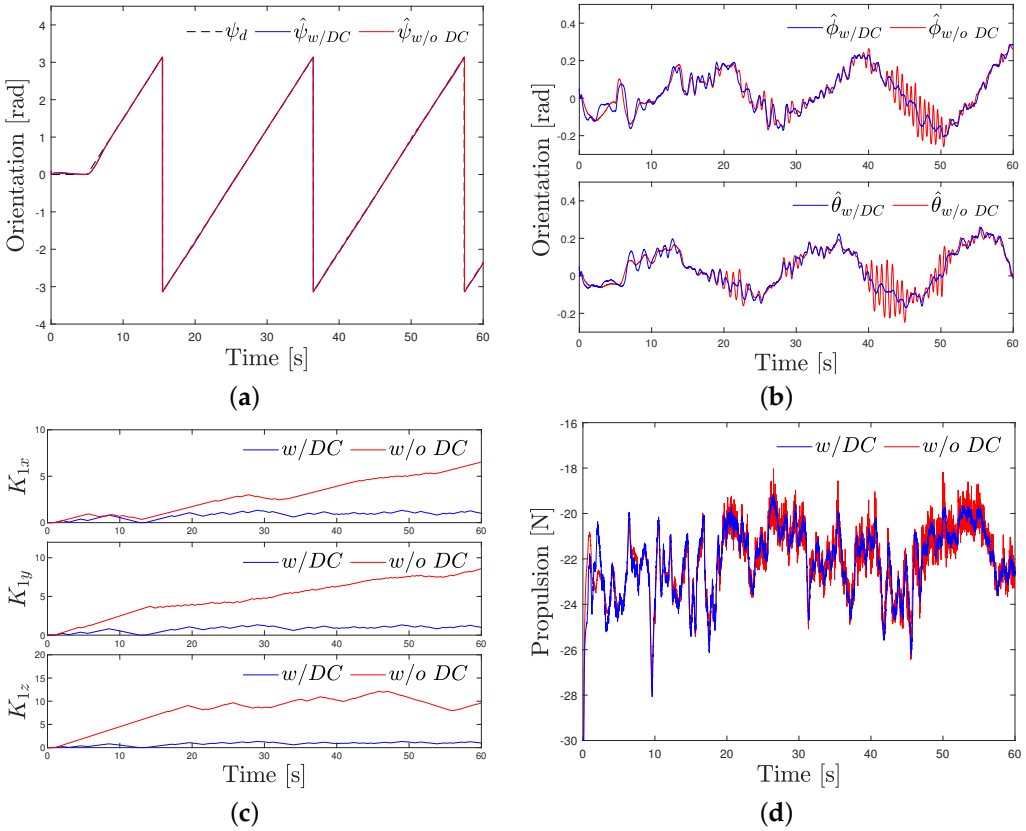

Figure 6. Disturbance compensation analysis. Attitude performance and control input evolution. (**a**) Yaw angle (**b**) Roll and pitch responses, (**c**) Adaptive gains, (**d**) Thrust.

The evolution of the adaptive gains for the positioning subsystem is portrayed in Figure 6c. Naturally, the feedback regulation-based controller requires higher magnitudes from the adaptive gains. Moreover, we note that K_{1x} and K_{1y} exhibited an increasing tendency, whereas the needed effort from K_{1z} was significantly larger than the perturbation rejection-based approach. As a consequence, the control input related to the total motor thrust leaned towards presenting chattering, as seen in Figure 6d. Therefore, the implementation of a disturbance compensation action in the control input of the system improves the trajectory execution of the UAV and aids in keeping a lower value from the adaptive gains of the controller while attenuating the chattering phenomenon in exchange for a regularly larger control input magnitude.

5.2. Comparison Study

The operation of the proposed FxtESO-based control strategy was compared with the nonlinear extended state observer-based adaptive sliding mode controller (NESO-ASMC) from [56] described by NESO:

$$\dot{\hat{\xi}}_1 = \hat{\xi}_2 - Q_1 f(\tilde{\xi}), \tag{79}$$

$$\dot{\hat{\xi}}_2 = \hat{\xi}_3 - Q_2 f(\tilde{\xi}), \tag{80}$$

$$\dot{\hat{\xi}}_3 = -Q_3 f(\tilde{\xi}), \tag{81}$$

with

$$f(\tilde{\xi}) = \begin{cases} |\xi_1 - \hat{\xi}_1|^{\iota} \text{sign}(\xi_1 - \hat{\xi}_1) & \text{if } |\xi_1 - \hat{\xi}_1| > \Lambda \\ \frac{\xi_1 - \hat{\xi}_1}{\Lambda^{1-\iota}} & \text{if } |\xi_1 - \hat{\xi}_1| \leq \Lambda \end{cases} \tag{82}$$

and the auxiliary control strategy

$$\nu = -\varsigma_1 \text{sig}^{1/2}(\sigma) - \int \frac{\varsigma_2}{2} \text{sign}(\sigma), \tag{83}$$

where $\varsigma_2 = \varsigma_3 \varsigma_1$, $\varsigma_3 > 0$, and the adaptability law is

$$\dot{\varsigma}_1 = \begin{cases} \varsigma_4 \text{sign}(|\sigma| - \mu_\varsigma) & \varsigma_1 > \varsigma_{\min} \\ \varsigma_{\min} & \varsigma_1 \leq \varsigma_{\min} \end{cases}. \tag{84}$$

For comparative analysis, the NESO-based ASMC parameters were chosen as $Q_{1q} = 20$, $Q_{2q} = 247$, $Q_{3q} = 1500$, $\iota_q = 0.7$, and $\Lambda_q = 0.05$ for $q = \{x, y, z, \phi, \theta, \psi\}$, $\varsigma_{3x} = \varsigma_{3y} = 0.01$, $\varsigma_{3z} = 0.2$, $\varsigma_{4x} = \varsigma_{4y} = 0.5$, $\varsigma_{4z} = 3$, $\varsigma_{\min_x} = \varsigma_{\min_y} = 0.01$, $\varsigma_{\min_z} = 0.1$, $\mu_{\varsigma_x} = \mu_{\varsigma_y} = \mu_{\varsigma_z} = 0.05$, $\varsigma_{3\phi} = \varsigma_{3\theta} = 0.3$, $\varsigma_{3\psi} = 1$, $\varsigma_{4\phi} = \varsigma_{4\theta} = \varsigma_{4\psi} = 1$, $\varsigma_{\min_\phi} = \varsigma_{\min_\theta} = \varsigma_{\min_\psi} = 0.1$, and $\mu_{\varsigma_\phi} = \mu_{\varsigma_\theta} = \mu_{\varsigma_\psi} = 0.05$.

The evolution of the disturbance estimation errors from both observer-based methods is displayed in Figure 7. Although their estimation performance under sensor noise conditions is accurate, we can notice that the NESO provided a larger peaking phenomenon than the fixed-time observer (see $\tilde{\xi}_{3z}$) due to the initial estimation error $\tilde{\xi}_z = 0.1$ and the UAV mass uncertainty. As a consequence, Figure 8a shows that the FxtESO-based ASMC granted a more accurate trajectory tracking response with lower-amplitude oscillations at some points of the operation. Additionally, the trajectory execution in the z-axis from Figure 8b clearly portrays the effects of the peaking phenomenon on the NESO-based ASMC since the quadrotor was not able to take off as fast as the vehicle driven by the FxtESO-ASMC. Furthermore, the displayed trajectories along the x and y from Figure 8c,d demonstrate that the proposed method offered stronger robustness specifically during the hover flight stage of the trajectory where the NESO-ASMC presented deviations between 1 and 3 m. The effect of prior errors in the attitude subsystem is given in Figure 8e. We notice that, unlike in the proposed approach, the influence of the total disturbance in the system caused the quadrotor managed under the NESO-ASMC execute high-frequency rotations within the first 10 s of the simulation. On the other hand, Figure 8f illustrates that both observer-based controllers provided an effective tracking of the desired heading.

The state estimation performance of the employed observers for the yaw output is given in Figure 9a. Despite the presence of sensor noise and model uncertainties, both methods achieved the real state within 0.5 s. However, the proposed FxtESO offered smoother and more straightforward state tracking since it did not present any overshoot. The evolution of the positioning subsystem adaptive gains is illustrated in Figure 9b. At the start of the simulation, the FxtESO-ASMC approach required approximately 400% less magnitudes of K_{1x}, K_{1y}, and K_{1z} than the NESO-ASMC scheme. Furthermore, at time $t > 20$, the adjustments of parameters K_{1x} and K_{1y} from both observer-based controllers gradually settled down and stayed at a range of values denoted by [0.5,2). Regarding adaptive gain K_{1z} at $t > 20$, it is easy to note that it had a more active evolution under the NESO-ASMC algorithm, whereas the same parameter from the FxtESO-ASMC kept within the same magnitude interval as K_{1x} and K_{1y}. The applied control inputs for the quadrotor are portrayed in Figure 9c,d, respectively. The thrust provided by the NESO-ASMC at time $0 < t \leq 5$ shows the effect of the peaking phenomenon on the propulsion of the system. While the signal from the FxtESO-ASMC showed no peaking. Moreover, it allowed operation of the rotorcraft with an average thrust of -22 N with few peaks between 26 and 28 N, which is suitable for a 2 kg vehicle. Finally, the advantage of the proposed approach with respect to the executed torques is evident. The fixed-time observer-based controller supplied rotational control inputs within the range of ± 0.1 Nm, which is available considering the determined characteristics of the UAV. On the other hand, the torques given by the NESO-based algorithm remained within the range of ± 0.3 Nm, including a few short-time spikes that reached ± 0.5 Nm.

A quantitative analysis for prior results is presented in Table 1. Performance indicators such as the mean squared error,

$$MSE = \frac{1}{N}\sum_{i=1}^{N} e_i^2, \text{ for } i = \{1, 2, \ldots, N\},$$

the root mean squared error,

$$RMSE = \sqrt{\frac{1}{N}\sum_{i=1}^{N} e_i^2}, \text{ for } i = \{1, 2, \ldots, N\},$$

the integral absolute error,

$$IAE = \int_0^T |e(t)|dt,$$

the integral squared error,

$$ISE = \int_0^T e(t)^2 dt,$$

and the integral time absolute error,

$$ITAE = \int_0^T |e(t)|tdt,$$

were employed to evaluate and corroborate the advantages of the proposed method. Statistically, it can be concluded that both observer-based strategies provided the same position estimation performance since their discrepancies in this aspect were not significant. However, the computed data show the superiority of the FxtESO-ASMC approach in the disturbance estimation and position error areas. Furthermore, the information related to the norm of control suggests that the adaptive fixed-time observer-based controller needed less control effort than the similar, NESO-based controller.

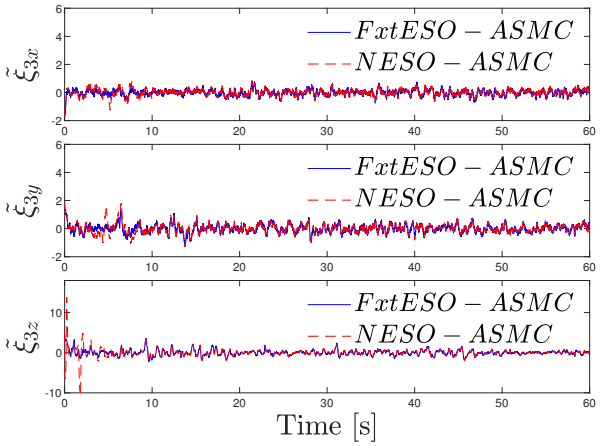

Figure 7. ESO−based controller comparison. Disturbance estimation error.

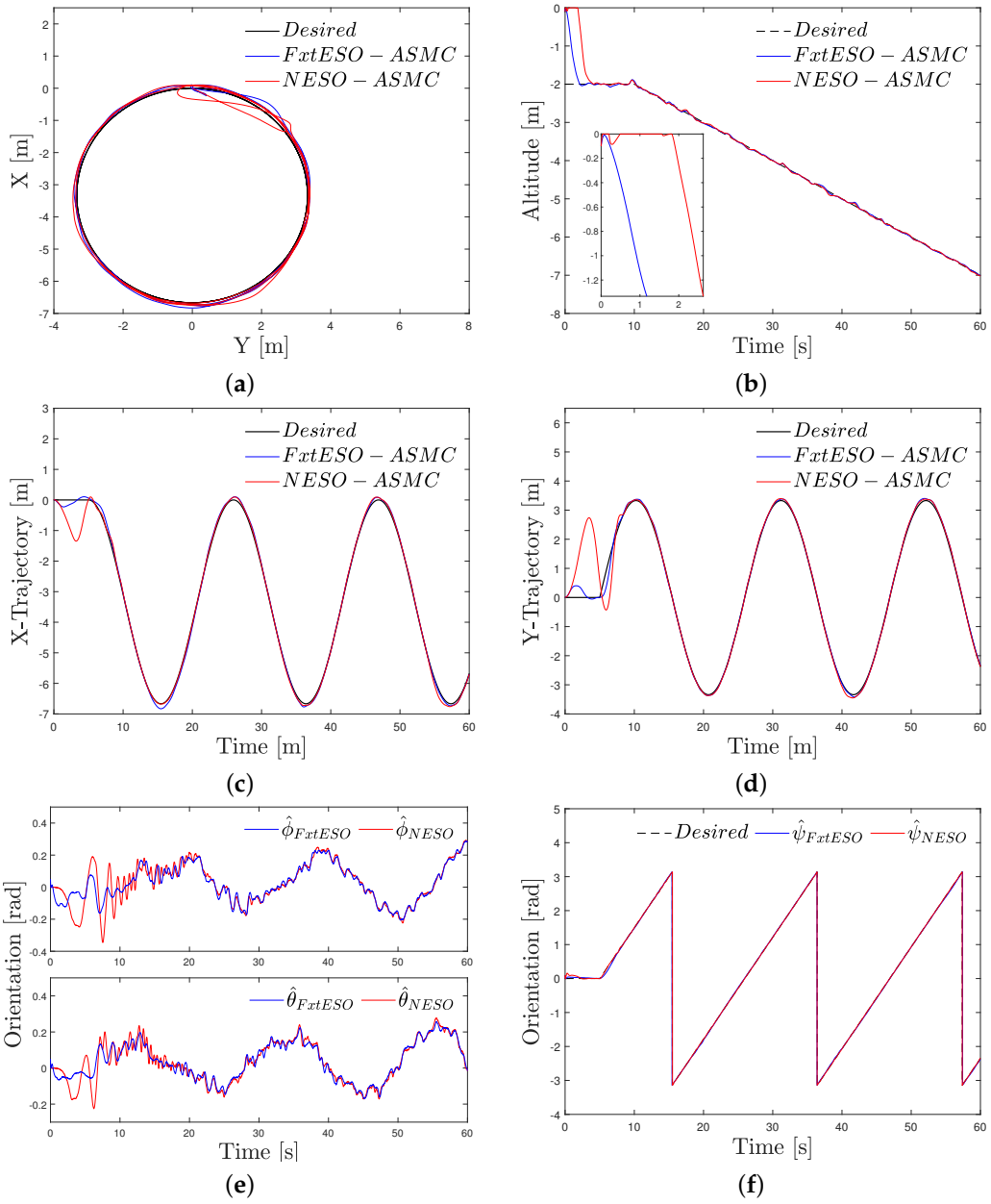

Figure 8. FxtESO and NESO−based adaptive controller comparison. Trajectory tracking: (**a**) top view, (**b**) z axis, (**c**) x response, (**d**) y behavior, (**e**) Roll and pitch estimation, (**f**) yaw estimation.

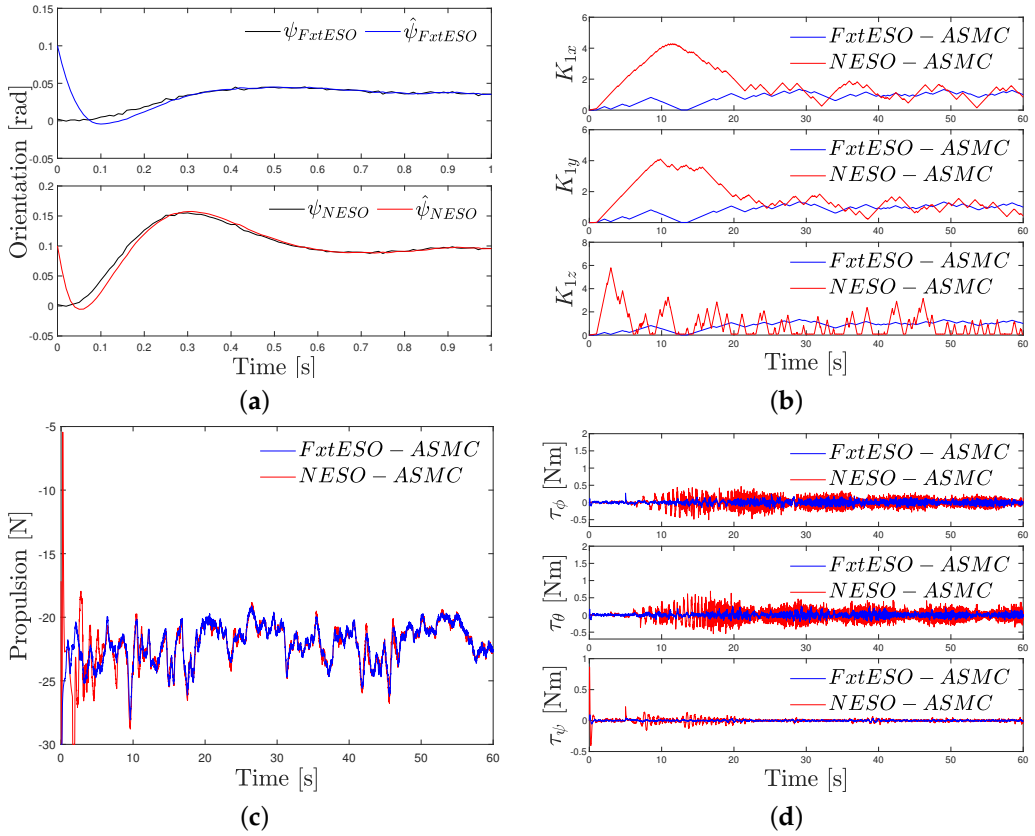

Figure 9. Quadrotor UAV trajectory. FxtESO and NESO−based adaptive controller comparison. (**a**) Yaw convergence, (**b**) Adaptive gains, (**c**) Required thrust, (**d**) Generated torques

Table 1. Quantitative analysis of the results.

	Disturbance Estimation				
	MSE	RMSE	IAE	ISE	ITAE
x-axis					
FxtESO-ASMC	**0.0469**	**0.2166**	**9.9390**	**2.8160**	**302.7**
NESO-ASMC	0.0586	0.2421	11.00	3.5190	305.2
y-axis					
FxtESO-ASMC	**0.0875**	**0.2958**	**13.51**	**5.25**	377.2
NESO-ASMC	0.1059	0.3254	14.34	6.3550	**364.6**
z-axis					
FxtESO-ASMC	**0.4698**	**0.6854**	**29.25**	**28.19**	729.3
NESO-ASMC	1.0988	1.0482	33.37	65.94	**699.5**
	Position Estimation				
	MSE	RMSE	IAE	ISE	ITAE
x-axis					
FxtESO-ASMC	1.41×10^{-6}	1.19×10^{-3}	0.0569	8.50×10^{-5}	1.7110
NESO-ASMC	$\mathbf{1.38 \times 10^{-6}}$	$\mathbf{1.17 \times 10^{-3}}$	**0.0562**	$\mathbf{8.30 \times 10^{-5}}$	**1.6484**
y-axis					
FxtESO-ASMC	1.43×10^{-6}	1.19×10^{-3}	0.0572	8.62×10^{-5}	1.7180
NESO-ASMC	$\mathbf{1.40 \times 10^{-6}}$	$\mathbf{1.18 \times 10^{-3}}$	**0.0565**	$\mathbf{8.43 \times 10^{-5}}$	**1.69**
z-axis					
FxtESO-ASMC	$\mathbf{5.43 \times 10^{-6}}$	$\mathbf{2.33 \times 10^{-3}}$	**0.0655**	$\mathbf{3.26 \times 10^{-4}}$	1.799
NESO-ASMC	6.95×10^{-6}	2.63×10^{-3}	0.0697	4.17×10^{-4}	**1.768**

Table 1. *Cont.*

Quadrotor UAV Position					
	MSE	RMSE	IAE	ISE	ITAE
x-axis					
FxtESO-ASMC	**0.0075**	**0.0866**	**4.1990**	**0.4472**	**104.3**
NESO-ASMC	0.0566	0.2379	6.0870	3.3990	114.7
FxtESO-ASMC w/o DC	0.0413	0.2032	9.186	2.481	234.9
y-axis					
FxtESO-ASMC	**0.0111**	**0.1054**	**3.5910**	**0.6640**	**77.02**
NESO-ASMC	0.2925	0.5408	11.65	17.55	117.30
FxtESO-ASMC w/o DC	0.0536	0.2315	8.7970	3.214	153.8
z-axis					
FxtESO-ASMC	**0.0465**	**0.2156**	**3.1020**	**2.7910**	**34.13**
NESO-ASMC	0.1499	0.3872	6.0870	8.9940	39.97
FxtESO-ASMC w/o DC	0.0917	0.3028	8.0420	5.50	77.95
Quadrotor UAV. Norms of Control					
	$\|T_h\|$	$\|\boldsymbol{\tau}\|$			
FxtESO-ASMC	1717.70	395.9815			
NESO-ASMC	1721.80	1041.7			
FxtESO-ASMC w/o DC	1716.80	785.2556			

6. Conclusions

A fixed-time extended state observer-based adaptive sliding mode control was designed for driving a quadrotor UAV subject to severe-intensity turbulent wind gusts while tracking a spiral trajectory. The external disturbances, denoted by the Von Karman wind model, and the effects of model uncertainties regarding the angular dynamics and the mass of the rotorcraft were rejected via fixed-time augmented state estimation and feedback control loop compensation, regardless of the initial conditions of the system. Furthermore, the adaptive gain from the controller allowed the usage of the necessary control input, preserving robustness. Moreover, the closed-loop system stability was guaranteed by means of Lyapunov theory. Finally, simulations in Simulink/Matlab demonstrated the advantages of disturbance compensation in improving the performance of the UAV and the effectiveness of the proposed control scheme by making comparisons against a nonlinear extended state observer-based adaptive controller.

Author Contributions: Conceptualization, A.M.-M., H.C. and H.W.; methodology, A.M.-M. and H.C.; software, A.M.-M.; validation, H.C. and H.W.; writing—original draft preparation, A.M.-M.; writing—review and editing, A.M.-M., H.C. and H.W. All authors have read and agreed to the published version of the manuscript.

Funding: This research received no external funding.

Institutional Review Board Statement: Not applicable.

Data Availability Statement: The data is contained within the article.

Acknowledgments: We thank Multi-Robot System Laboratory of the Tecnologico de Monterrey, and the CONACyT scholarship for support in the development of this project.

Conflicts of Interest: The authors declare no conflict of interest.

Abbreviations

The following abbreviations are used in this manuscript:

ASMC	Adaptive sliding mode control
ESO	Extended state observer
FxtESO	Fixed-time extended state observer
NESO	Nonlinear extended state observer
UAV	Unamnned Aerial Vehicle

References

1. Najm, A.A.; Ibraheem, I.K. Nonlinear PID controller design for a 6-DOF UAV quadrotor system. *Eng. Sci. Technol. Int. J.* **2019**, *22*, 1087–1097. [CrossRef]
2. Zhou, L.; Zhang, J.; She, H.; Jin, H. Quadrotor UAV flight control via a novel saturation integral backstepping controller. *Automatika* **2019**, *60*, 193–206. [CrossRef]
3. Labbadi, M.; Cherkaoui, M. Robust adaptive backstepping fast terminal sliding mode controller for uncertain quadrotor UAV. *Aerosp. Sci. Technol.* **2019**, *93*, 105306. [CrossRef]
4. Labbadi, M.; Cherkaoui, M.; houm, Y.E.; Guisser, M. Modeling and robust integral sliding mode control for a quadrotor unmanned aerial vehicle. In Proceedings of the 2018 IEEE 6th International Renewable and Sustainable Energy Conference (IRSEC), Rabat, Morocco, 5–8 December 2018; 2018; pp. 1–6.
5. Nekoukar, V.; Dehkordi, N.M. Robust path tracking of a quadrotor using adaptive fuzzy terminal sliding mode control. *Control. Eng. Pract.* **2021**, *110*, 104763. [CrossRef]
6. Li, S.; Yang, J.; Chen, W.H.; Chen, X. *Disturbance Observer-Based Control: Methods and Applications*; CRC Press: Boca Raton, FL, USA, 2014.
7. Miranda-Moya, A.; Castañeda, H.; Wang, H. Turbulent Wind Gusts Estimation and Compensation via High-Gain Extended Observer-based Adaptive Sliding Mode for a Quadrotor UAV. In Proceedings of the IEEE 2021 International Conference on Unmanned Aircraft Systems (ICUAS), Athens, Greece, 15–18 June 2021; pp. 476–481.
8. Davoudi, B.; Taheri, E.; Duraisamy, K.; Jayaraman, B.; Kolmanovsky, I. Quad-rotor flight simulation in realistic atmospheric conditions. *AIAA J.* **2020**, *58*, 1992–2004. [CrossRef]
9. Gao, Z.; Guo, G. Command-filtered fixed-time trajectory tracking control of surface vehicles based on a disturbance observer. *Int. J. Robust Nonlinear Control.* **2019**, *29*, 4348–4365. [CrossRef]
10. Lyu, X.; Zhou, J.; Gu, H.; Li, Z.; Shen, S.; Zhang, F. Disturbance Observer Based Hovering Control of Quadrotor Tail-sitter VTOL UAVs Using H_∞ Synthesis. *IEEE Robot. Autom. Lett.* **2018**, *3*, 2910–2917. [CrossRef]
11. Wu, K.; Fan, B.; Zhang, X. Trajectory following control of UAVs with wind disturbance. In Proceedings of the 2017 36th Chinese Control Conference (CCC), Dalian, China 26–28 June 2017; pp. 4993–4997.
12. Yu, G.; Chen, Y.; Chen, Z.; Wu, H.; Cheng, L. Design of terminal sliding mode controller for a quadrotor UAV with disturbance observer. In Proceedings of the 2020 IEEE 39th Chinese Control Conference (CCC), Shenyang, China, 27–29 July 2020; pp. 2072–2077.
13. Qin, L.; Zhou, W.; Li, L.; Jiang, W. Active disturbance rejection control system design for quadrotor. In Proceedings of the 2017 36th Chinese Control Conference (CCC), Dalian, China 26–28 June 2017; pp. 6530–6534.
14. Wu, C.; Yan, J.; Lin, H.; Wu, X.; Xiao, B. Fixed-time disturbance observer-based chattering-free sliding mode attitude tracking control of aircraft with sensor noises. *Aerosp. Sci. Technol.* **2021**, *111*, 106565. [CrossRef]
15. Wu, S.; Chen, L.; Zhang, D.; Chen, J.; Shao, X. Disturbance observer based fixed time sliding mode control for spacecraft proximity operations with coupled dynamics. *Adv. Space Res.* **2020**, *66*, 2179–2193. [CrossRef]
16. Wang, X.; Guo, J.; Tang, S.; Qi, S. Fixed-time disturbance observer based fixed-time back-stepping control for an air-breathing hypersonic vehicle. *ISA Trans.* **2019**, *88*, 233–245. [CrossRef]
17. Smith, J.; Su, J.; Liu, C.; Chen, W.H. Disturbance observer based control with anti-windup applied to a small fixed wing UAV for disturbance rejection. *J. Intell. Robot. Syst.* **2017**, *88*, 329–346. [CrossRef]
18. *MIL-STD-1797A*; Department of Defense Handbook: Flying Qualities of Piloted Aircraft. University Reprints 2017; Department of Defense, Washington, DC, USA, 1995.
19. Rodriguez-Mata, A.E.; Gonzalez-Hernandez, I.; Rangel-Peraza, J.G.; Salazar, S.; Leal, R.L. Wind-gust compensation algorithm based on high-gain residual observer to control a quadrotor aircraft: real-time verification task at fixed point. *Int. J. Control. Autom. Syst.* **2018**, *16*, 856–866. [CrossRef]
20. Zhang, Z.; Wang, F.; Guo, Y.; Hua, C. Multivariable sliding mode backstepping controller design for quadrotor UAV based on disturbance observer. *Sci. China Inf. Sci.* **2018**, *61*, 112207. [CrossRef]
21. Aboudonia, A.; Rashad, R.; El-Badawy, A. Time domain disturbance observer based control of a quadrotor unmanned aerial vehicle. In Proceedings of the 2015 XXV International Conference on Information, Communication and Automation Technologies (ICAT), Sarajevo, Bosnia and Herzegovina, 29–31 October 2015; pp. 1–6.
22. Aboudonia, A.; El-Badawy, A.; Rashad, R. Disturbance observer-based feedback linearization control of an unmanned quadrotor helicopter. *Proc. Inst. Mech. Eng. Part J. Syst. Control. Eng.* **2016**, *230*, 877–891. [CrossRef]

23. Aboudonia, A.; Rashad, R.; El-Badawy, A. Composite hierarchical anti-disturbance control of a quadrotor UAV in the presence of matched and mismatched disturbances. *J. Intell. Robot. Syst.* **2018**, *90*, 201–216. [CrossRef]
24. Han, J. From PID to active disturbance rejection control. *IEEE Trans. Ind. Electron.* **2009**, *56*, 900–906. [CrossRef]
25. Wang, H.; Li, N.; Wang, Y.; Su, B. Backstepping sliding mode trajectory tracking via extended state observer for quadrotors with wind disturbance. *Int. J. Control. Autom. Syst.* **2021**, *19*, 3273–3284. [CrossRef]
26. Shao, X.; Liu, J.; Cao, H.; Shen, C.; Wang, H. Robust dynamic surface trajectory tracking control for a quadrotor UAV via extended state observer. *Int. J. Robust Nonlinear Control.* **2018**, *28*, 2700–2719. [CrossRef]
27. Zhiyuan, C.; Yanyang, L.; Yanhua, S.; Hongyu, C.; Bin, W.; Mingqi, H.; Rao, Y. Fuzzy sliding mode control for rotorcraft aerial manipulator with extended state observer. In Proceedings of the 2020 IEEE: Chinese Automation Congress (CAC), Shanghai, China, 6–8 November 2020; pp. 1710–1714.
28. Khalil, H.K. Extended high-gain observers as disturbance estimators. *Sice J. Control. Meas. Syst. Integr.* **2017**, *10*, 125–134. [CrossRef]
29. Liu, J.; Sun, M.; Chen, Z.; Sun, Q. Super-twisting sliding mode control for aircraft at high angle of attack based on finite-time extended state observer. *Nonlinear Dyn.* **2020**, *99*, 2785–2799. [CrossRef]
30. Polyakov, A. Nonlinear feedback design for fixed-time stabilization of linear control systems. *IEEE Trans. Autom. Control.* **2011**, *57*, 2106–2110. [CrossRef]
31. Biao, T.; Xingling, S.; Wei, Y.; Wendong, Z. Fixed time output feedback containment for uncertain nonlinear multiagent systems with switching communication topologies. *ISA Trans.* **2021**, *111*, 82–95. [CrossRef] [PubMed]
32. Hu, D.; Zhang, S.; Zou, A.M. Velocity-free fixed-time attitude cooperative control for spacecraft formations under directed graphs. *Int. J. Robust Nonlinear Control.* **2021**, *31*, 2905–2927. [CrossRef]
33. Cui, L.; Jin, N.; Chang, S.; Zuo, Z.; Zhao, Z. Fixed-time ESO based fixed-time integral terminal sliding mode controller design for a missile. *ISA Trans.* **2021**, *125*, 237–251. [CrossRef]
34. Jin, R.; Rocco, P.; Geng, Y. Observer-based fixed-time tracking control for space robots in task space. *Acta Astronaut.* **2021**, *184*, 35–45. [CrossRef]
35. Mechali, O.; Xu, L.; Huang, Y.; Shi, M.; Xie, X. Observer-based fixed-time continuous nonsingular terminal sliding mode control of quadrotor aircraft under uncertainties and disturbances for robust trajectory tracking: Theory and experiment. *Control. Eng. Pract.* **2021**, *111*, 104806. [CrossRef]
36. Li, B.; Ban, H.; Gong, W.; Xiao, B. Extended state observer-based finite-time dynamic surface control for trajectory tracking of a quadrotor unmanned aerial vehicle. *Trans. Inst. Meas. Control* **2020**, *42*, 2956–2968. [CrossRef]
37. Liu, J.; Sun, M.; Chen, Z.; Sun, Q. Output feedback control for aircraft at high angle of attack based upon fixed-time extended state observer. *Aerosp. Sci. Technol.* **2019**, *95*, 105468. [CrossRef]
38. Khalil, H.K. *Nonlinear Systems*, 3rd ed.; Prentice Hall: Upper Saddle River, NJ, USA, 2002; Volume 115.
39. Fridman, L.; Barbot, J.P.; Plestan, F. Recent trends in sliding mode control. In *IET Control, Robotics 552 and Sensors Series Volume 102*; The Institution of Engineering and Technology: London, UK; 2016.
40. Zhu, Z.; Xia, Y.; Fu, M. Attitude stabilization of rigid spacecraft with finite-time convergence. *Int. J. Robust Nonlinear Control.* **2011**, *21*, 686–702. [CrossRef]
41. Zhang, J.; Yu, S.; Yan, Y. Fixed-time output feedback trajectory tracking control of marine surface vessels subject to unknown external disturbances and uncertainties. *ISA Trans.* **2019**, *93*, 145–155. [CrossRef]
42. Polyakov, A.; Fridman, L. Stability notions and Lyapunov functions for sliding mode control systems. *J. Frankl. Inst.* **2014**, *351*, 1831–1865. [CrossRef]
43. Perruquetti, W.; Floquet, T.; Moulay, E. Finite-time observers: application to secure communication. *IEEE Trans. Autom. Control.* **2008**, *53*, 356–360. [CrossRef]
44. Bhat, S.P.; Bernstein, D.S. Geometric homogeneity with applications to finite-time stability. *Math. Control. Signals Syst.* **2005**, *17*, 101–127. [CrossRef]
45. Wang, H.; Chen, B.; Lin, C.; Sun, Y.; Wang, F. Adaptive finite-time control for a class of uncertain high-order non-linear systems based on fuzzy approximation. *IET Control. Theory Appl.* **2017**, *11*, 677–684. [CrossRef]
46. Castañeda, H.; Gordillo, J.L. Spatial Modeling and Robust Flight Control Based on Adaptive Sliding Mode Approach for a Quadrotor MAV. *J. Intell. Robot. Syst.* **2019**, *93*, 101–111. [CrossRef]
47. Gage, S. Creating a unified graphical wind turbulence model from multiple specifications. In Proceedings of the AIAA Modeling and Simulation Technologies Conference and Exhibit, Austin, TX, USA, 1–14 August 2003; p. 5529.
48. Zhang, J.; Yu, S.; Yan, Y.; Wu, D. Fixed-time output feedback sliding mode tracking control of marine surface vessels under actuator faults with disturbance cancellation. *Appl. Ocean. Res.* **2020**, *104*, 102378. [CrossRef]
49. Castañeda, H.; Rodriguez, J.; Gordillo, J.L. Continuous and smooth differentiator based on adaptive sliding mode control for a quad-rotor MAV. *Asian J. Control.* **2019**, *23*, 661–672. [CrossRef]
50. Zhang, L.; Wei, C.; Wu, R.; Cui, N. Fixed-time extended state observer based non-singular fast terminal sliding mode control for a VTVL reusable launch vehicle. *Aerosp. Sci. Technol.* **2018**, *82*, 70–79. [CrossRef]
51. Basin, M.; Yu, P.; Shtessel, Y. Finite-and fixed-time differentiators utilising HOSM techniques. *IET Control. Theory Appl.* **2017**, *11*, 1144–1152. [CrossRef]

52. Zhang, J.; Yu, S.; Yan, Y. Fixed-time extended state observer-based trajectory tracking and point stabilization control for marine surface vessels with uncertainties and disturbances. *Ocean. Eng.* **2019**, *186*, 106109. [CrossRef]
53. Tian, B.; Zuo, Z.; Yan, X.; Wang, H. A fixed-time output feedback control scheme for double integrator systems. *Automatica* **2017**, *80*, 17–24. [CrossRef]
54. Plestan, F.; Shtessel, Y.; Bregeault, V.; Poznyak, A. New methodologies for adaptive sliding mode control. *Int. J. Control.* **2010**, *83*, 1907–1919. [CrossRef]
55. Khalil, H.K. *High-Gain Observers in Nonlinear Feedback Control*; SIAM: Philadelphia, PA, USA, 2017.
56. Castañeda, H.; Salas-Peña, O.S.; de León-Morales, J. Extended observer based on adaptive second order sliding mode control for a fixed wing UAV. *ISA Trans.* **2017**, *66*, 226–232. [CrossRef] [PubMed]